The Journal of Chemical Physics

Ultrafast relaxation dynamics of $Au_{38}(SC_6H_{13})_{24}$ monolayer-protected clusters resolved by two-dimensional electronic spectroscopy

Cite as: J. Chem. Phys. **155**, 124303 (2021); https://doi.org/10.1063/5.0056832
Submitted: 14 May 2021 . Accepted: 03 September 2021 . Published Online: 23 September 2021

William R. Jeffries, Jordan L. Wallace and Kenneth L. Knappenberger

The Journal of Chemical Physics ARTICLE scitation.org/journal/jcp

Ultrafast relaxation dynamics of $Au_{38}(SC_6H_{13})_{24}$ monolayer-protected clusters resolved by two-dimensional electronic spectroscopy

Cite as: J. Chem. Phys. 155, 124303 (2021); doi: 10.1063/5.0056832
Submitted: 14 May 2021 • Accepted: 3 September 2021 •
Published Online: 23 September 2021

William R. Jeffries, Jordan L. Wallace, and Kenneth L. Knappenberger Jr.[a)]

AFFILIATIONS

Department of Chemistry, The Pennsylvania State University, University Park, Pennsylvania 16802, USA

Note: This paper is part of the JCP Special Topic on From Atom-Precise Nanoclusters to Superatom Materials.
[a)]**Author to whom correspondence should be addressed:** klk260@psu.edu

ABSTRACT

Electronic relaxation dynamics of neutral $Au_{38}(SC_6H_{13})_{24}$ monolayer-protected clusters (MPCs), following excitation of the mixed 15 875 cm^{-1} charge transfer resonance, were studied using femtosecond transient absorption (fsTA) and two-dimensional electronic spectroscopy (2DES). The excited carriers relax by three different mechanisms, including an ~100 fs $HOMO_{-12/-13}$ to $HOMO_{-4/-6}$ hole transfer, picosecond $HOMO_{-4/-6}$ to HOMO hole transfer, and subsequent electron–hole recombination that persisted beyond the hundreds of picoseconds measurement range. The fsTA data revealed two transient bleach components at 15 820 and 15 625 cm^{-1}, where the lower frequency component exhibited a delayed first-order buildup of 80 ± 25 fs that matched the decay of the high-energy bleach component (110 ± 45 fs). These results suggested that the excited charge carriers internally relax within the exited-state manifold in ≈100 fs. 2DES resolved multiple electronic fine-structure transient peaks that spanned excitation frequencies ranging from 15 500 to 16 100 cm^{-1}. State-to-state dynamics were understood by the analysis of time-dependent 2DES transient signal amplitudes at numerous excitation-detection frequency combinations. An off-diagonal cross peak at 15 825–15 620 cm^{-1} excitation-detection signified the $HOMO_{-12/-13}$ to $HOMO_{-4/-6}$ hole transfer process. The lowest-frequency (15 620 cm^{-1}) 2DES diagonal fine-structure peak exhibited instantaneous amplitude but intensified following a 75 ± 10 fs buildup when compared to diagonal peaks at higher frequencies. This observation indicated that the charge transfer resonance in $Au_{38}(SC_6H_{13})_{24}$ MPCs is comprised of several electronic transitions of unique spectral weights, which may result from different orbital contributions associated with specific cluster domains. The use of 2DES in combination with structurally precise MPCs can provide a platform for understanding structure-dependent electronic dynamics in metal nanoclusters and technologically important metal–chalcogenide interfaces.

I. INTRODUCTION

Monolayer-protected clusters (MPCs) are a class of structurally well-defined colloidal metals. In some instances, atomic-level structural control has been reported. Many MPCs exhibit discrete optical transitions and electronic relaxation dynamics. In fact, some gold MPC compositions are known to exhibit spin-polarized photoluminescence and electronic-spin-state-conversion dynamics.[1–4] Hence, understanding the electron dynamics of MPC quantum-confined states may provide insights for how atomic precision can be leveraged for quantum sciences and other photonic applications. Other potential applications for MPCs include photocatalysis,[5–7] medical imaging,[8] nonlinear frequency conversion,[9,10] and molecular catalysis,[11,12] among others.

The optical properties and electron dynamics of MPCs can be influenced by cluster structure and composition, which are generally described by three motifs. These components include (i) an all-metal atom core, (ii) an inorganic semiring that consists of alternating Au–S units, and (iii) organic passivating ligands.[13–19] One MPC that has been isolated and structurally characterized is $Au_{38}(SC_2H_4Ph)_{24}$, which exists as two distinct isomers.[18,19] First reports based on x-ray crystallographic structure determination described a face-centered bi-icosahedral 23-gold-atom core that is protected by three $Au(SR)_2$ monomeric and six $Au_2(SR)_3$ dimeric staple-like surface motifs; SR denotes an alkanethiol. This structure is often referred to as the $Au_{38}Q$ isomer.[19] More recently, a structure of higher symmetry—the $Au_{38}T$ isomer—was reported.[18] The $Au_{38}T$ isomer also consists of an Au_{23} core, but it consists of an

Au_{13} icosahedron and an Au_{12} tri-tetrahedron, which is protected by three $Au_2(SR)_3$, three $Au(SR)_2$, two $Au_3(SR)_4$, and one SR bridge staple units. In addition to structure, the two isomers exhibit distinct electronic absorption spectra. In particular, the $Au_{38}Q$ isomer supports mixed charge transfer excitation at 15 870 cm^{-1}, where excitation occurs from the metal–organic staple units to the all-metal cluster core.[18] The $Au_{38}T$ isomer shows a weak absorption peak at 14 100 cm^{-1}.[18] It was recently determined that both metal core and ligand structure directly impact charge carrier lifetimes for MPCs containing ~38 gold atoms. Electronic relaxation on the picosecond timescale is accelerated for the $Au_{38}T$ isomer compared to $Au_{38}Q$.[20] Zhou *et al.* determined that 1-adamantanethiolated $Au_{38}S_2(S\text{-}Adm)_{20}$ nanoclusters have a 4.6 μs carrier lifetime, which is nearly 5000 times longer than the 1 ns lifetime of $Au_{30}(S\text{-}Adm)_{18}$ nanoclusters—despite their similar bandgap energies.[21] The authors attributed the large discrepancy in carrier lifetimes to crystal packing within the metal core structures. Temperature-dependent photoluminescence (TDPL) measurements also revealed that vibrationally mediated nonradiative relaxation channels selectively reduce quantum yields for high-energy emission states in both $Au_{25}(SC_8H_9)_{18}$ and $Au_{38}(SC_{12}H_{25})_{24}$ MPCs[22] due to preferential coupling to Au(I)–S stretches of the gold-chalcogenide semiring unit. Thus, the inorganic semiring and metal core structures play influential roles in determining electronic relaxation dynamics in quantum-confined MPCs.

Femtosecond transient absorption (fsTA) spectroscopy has been reliably used to obtain mechanistic understanding of carrier dynamics for many MPCs. These measurements include determining rates of discrete carrier relaxation in quantum-confined clusters and collective electronic cooling in metallic MPCs.[23–33] For the former, fsTA experiments on 25-gold-atom MPCs suggest that electronic relaxation occurs through rapid internal conversion (<200 fs) within the excited state manifold, which is followed by the picosecond metal-to-ligand charge migration.[23] A similar core–shell relaxation model for the 38-gold-atom system was recently proposed by Zhou *et al.*[20] The authors resolved a visible-to-near infrared (NIR) excitation-wavelength independent picosecond relaxation process attributed to a charge transfer step that precedes radiative recombination. The excitation-wavelength independence is notable because it implicates a charge transfer process involving the metal core atoms; NIR wavelengths are believed to excite transitions most heavily associated with the 23-gold-atom core. However, gold MPCs exhibit spectroscopic transitions derived from more than one structural domain,[34] whereas fsTA accurately resolves ultrafast relaxation rate constants, and the inherent spectral congestion due to the usage of broad-bandwidth, short-duration laser pulses makes it difficult to resolve the fine structure components of electronic state manifolds. Femtosecond two-dimensional electronic spectroscopy (2DES) is a third-order optical technique that provides excitation-detection spectral correlation while preserving the temporal resolution of ultrafast spectroscopy.[35–37] This time-resolved frequency correlation makes 2DES a sensitive tool for resolving state-to-state dynamics in quantum-confined systems, such as MPCs. Indeed, 2DES has been used for state-resolved studies of biological,[38–40] molecular,[41–43] and semiconductor systems.[44–48] Our group recently published the first description of 2DES-determined electronic relaxation dynamics in quantum-confined $Au_{25}(SC_8H_9)_{18}$ MPCs.[49] Specifically, 2DES was used to distinguish the sub-300 fs hot electron and hole relaxation within the superatom D and P states, respectively. These results demonstrate the power of 2DES to resolve state-specific electronic dynamics in quantum-confined metal nanoclusters.

Here, we describe electronic charge carrier relaxation dynamics of condensed-phase, quantum-confined neutral $Au_{38}(SC_6H_{13})_{24}$ nanoclusters using both fsTA and 2DES. We resolve multiple fine-structure peaks that uniquely contribute to internal conversion and charge transfer between organometallic staple units and the metal core of the cluster. These electronic relaxation events occurred on the 100 and 1000 fs timescales. Based on photoselection, these dynamics are attributed to the Au38Q isomer. A new finding—resolved only through the 2DES frequency correlation measurements—is state-to-state ($HOMO_{-12/-13}$ to $HOMO_{-4/-6}$) hole transfer. To the best of our knowledge, this is the first report of sub-picosecond dynamics in $Au_{38}(SR)_{24}$ MPCs and the first definitive determination of state-resolved dynamics for this system.

II. EXPERIMENTAL METHODS

The synthetic details and characterization were carried out following previously published protocols.[50] Briefly, the two-step synthesis was carried out as follows: first, L-glutathione-protected clusters were synthesized through combination of tetrachloroauric acid trihydrate dissolved in methanol and L-glutathione dissolved in water. The solution was stirred for ~30 min, which formed a yellow-brown suspension. A sodium borohydride solution in water was added, immediately turning the solution black. The solution was then stirred for 90 min. The crude material was washed with methanol several times and combined with 1-hexanethiol in a 1:1 water/acetone mixture. The solution was then stirred at 80 °C for 3 h. Finally, $Au_{38}(SC_6H_{12})_{24}$ clusters were separated from the aqueous phase and washed with methanol several times prior to being dissolved in chloroform for ultrafast experiments.

Details of the femtosecond time-resolved transient spectroscopy experimental setup have been described previously.[51] A schematic of the laser pulse sequence and experimental 2DES setup is shown in Fig. 1(a). In brief, 1040 nm fundamental pulses from a solid-state ytterbium amplifier (Spirit; Spectra-Physics) were modulated to a 100 kHz repetition rate and used to seed a noncollinear optical parametric amplifier (NOPA). The NOPA was used to generate visible pump and probe pulses centered at 630 nm with a FWHM of 36 nm, which equates to a transform limited pulse duration of 16 fs, which was achieved by pulse compression after frequency mixing. The pulses were collimated and sent to a pulse shaper-based 2DES QuickVisible setup (PhaseTech). Pump and probe pulses were generated and separated using a 90/10 (pump/probe) beam splitter. The pump beam was focused and spatially overlapped with the probe pulse at the sample after being temporally delayed using a mechanical delay stage. For 2DES measurements, the pump was dispersed using a grating and collimated by a parabolic mirror before being guided into an acousto-optic modulator (AOM), which was used to generate the two-pump pulse pair with a controlled time delay (t_1). A two-grating and two-parabolic mirror layout following the 4-*f* geometry was used to collect, modulate, and collimate the pump–pulse pair. A half-wave plate/polarizer was used to set the pump beam to the s-polarized configuration. The pump pulses

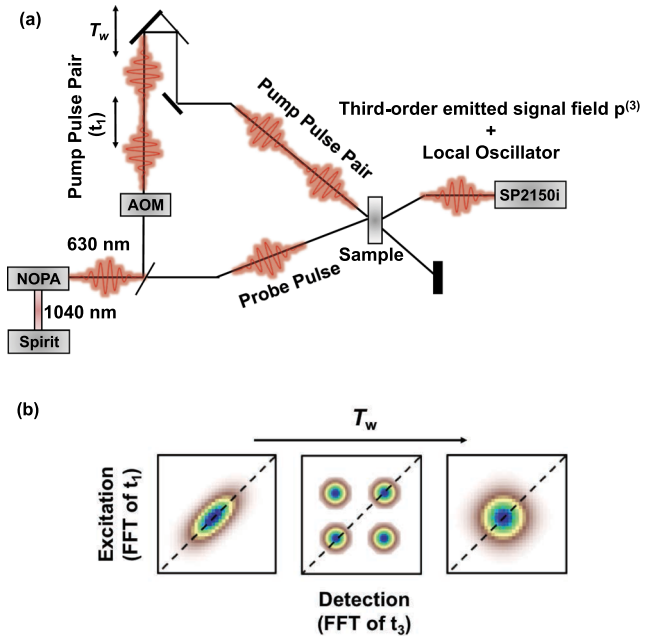

FIG. 1. (a) Experimental layout of the partially collinear pump–probe 2DES measurement geometry. A solid-state ytterbium amplifier (Spirit; Spectra-Physics) seeds a NOPA, which is used to generate femtosecond pulses at 630 nm. The pump–pulse pair is generated using an acoustic optical modulator (AOM; PhaseTech), and the emitted signal field was self-heterodyne detected using an SP2150i array detector (Princeton Instruments). (b) Generalized sequence of the 2DES maps that depict incoherent state-to-state carrier transfer, as described in the main text.

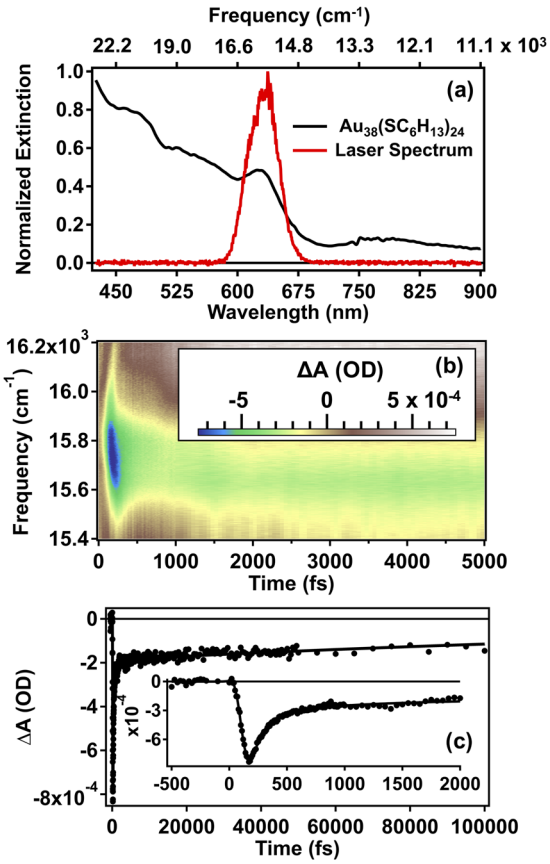

FIG. 2. (a) Linear extinction spectrum of $Au_{38}(SC_6H_{13})_{24}$ MPCs dissolved in chloroform overlaid with the femtosecond laser pulse. (b) The transient absorption map is false colored so that blue represents GSB and brown and white correspond to ESA. The transient map is plotted showing detection frequency spanning 15 400–16 200 cm^{-1} and pump–probe time delays up to 5000 fs. (c) The ultrafast dynamics at 15 750 cm^{-1} is shown for a pump–probe time delay of 100 000 fs. Fit results were obtained by fitting the transient signal to a series of exponentials convoluted with the Gaussian instrument response. The inset shows the bleach recovery dynamics within the first 2000 fs.

were temporally delayed using a mechanical delay stage to generate the pump–probe waiting time (T_w). The transmitted probe was dispersed and self-heterodyne detected using an SP2150i array detector (Princeton Instruments). The ultrafast 2DES measurements were conducted in the partially collinear pump–probe geometry, yielding the absorptive 2D spectra.[52,53]

Excitation-detection frequency correlations are detected in 2DES maps at a series of T_w values. The excitation axis is generated by Fourier transformation of the transient signal amplitude obtained vs t_1 at fixed T_w. The frequency axis is intrinsically Fourier transformed by use of an array detector. A sequence of generalized 2DES maps depicting an incoherent state-to-state carrier transfer mechanism is shown in Fig. 1(b). At the earliest T_w times [Fig. 1(b), left], the signal is distributed as a highly correlated diagonal peak, indicating the initially excited electronic transitions. As T_w is increased [Fig. 1(b), middle], off-diagonal cross peaks emerge in the 2DES maps, which reflect state-to-state carrier transfer. At the longest T_w times [Fig. 1(b), right], the transient signals take on a circular profile in the 2D correlation map, depicting thermalization of the charge carriers in the available manifold of states.

III. RESULTS AND DISCUSSION

The linear extinction spectrum of neutral $Au_{38}(SC_6H_{13})_{24}$ nanoclusters dispersed in chloroform is overlaid with the laser profile and is shown in Fig. 2(a). The extinction spectrum shows multiple absorption bands in the visible region of the electromagnetic spectrum. Specifically, the broad feature centered at ≈775 nm (≈12 900 cm^{-1}) is comprised of several transitions, including $HOMO_{-1} \rightarrow LUMO_{+1}$, $HOMO_{-2} \rightarrow LUMO_{+2}$, and $HOMO_{-3} \rightarrow LUMO$, all of which have significant Au (6sp) orbital character of atoms located within the bi-icosahedral core.[34,54] Unlike the lower energy features, the extinction peak centered at ≈630 nm (≈15 870 cm^{-1}) is comprised of several mixed transitions from core Au (6sp) and Au (5d) and S (3p) orbitals associated with the inorganic Au–S semiring (i.e., organometallic staple unit). These transitions include $HOMO \rightarrow LUMO_{+3}$, $HOMO_{-4/-6} \rightarrow LUMO$, and $HOMO_{-12/-13} \rightarrow LUMO$; the latter transition is predicted to carry the largest oscillator strength of this manifold.[34,54] Note that the core-localized $HOMO \rightarrow LUMO$ transition occurs at ≈1250 nm or ≈8000 cm^{-1} and is not considered in this study. The absorption spectrum shown in Fig. 2(a) is characteristic of the $Au_{38}Q$ isomer.

The 14 100 cm^{-1} absorption feature of $Au_{38}T$ is not prominent in Fig. 2(a). Furthermore, given that our experiments are characterized in a spectral range associated with $Au_{38}Q$ absorption, we attribute the observed dynamics to this isomer. In order to better understand electron dynamics of mixed states, including charge transfer character for MPCs, and metal–chalcogenide interfaces, in general, we selectively excited and monitored the charge transfer transition at 630 nm (15 870 cm^{-1}) that consists of multiple metal and ligand-based electronic excitations.

In order to understand the electron dynamics of the $Au_{38}(SC_6H_{13})_{24}$ manifold of states near 15 870 cm^{-1}, excited electronic relaxation rates were first determined from analysis of fsTA measurements. Figure 2(b) shows the transient absorption map obtained from near-degenerate excitation/detection by femtosecond laser pulses with a carrier wave of 630 nm (15 870 cm^{-1}). A negative amplitude signal corresponds to a decrease in the ground state population as carriers are excited into higher-lying excited states. A ground state bleach (GSB) signal appeared instantaneously at 15 750 cm^{-1} and subsequently recovered over the following hundreds of picoseconds. The recovery of the GSB, which corresponds to relaxation of the initially excited carriers, is shown by plotting the time-dependent amplitude at 15 750 cm^{-1} as a function of pump–probe time delay [Fig. 2(c)]. The bleach recovery dynamics were independent of laser power (Figs. S1 and S2). Therefore, the data were interpreted in the context of discrete molecular-like behavior, rather than the collective multi-carrier generation typical of large metallic nanoparticles. This finding was consistent with previous research on MPCs in this size range.[31] The GSB recovery was quantified by fitting the dynamics to exponential functions convoluted with the Gaussian instrument response. The fit results yielded a growth of 20 ± 5 fs, reflecting the instantaneous buildup of the signal, and two subsequent decay time constants of 120 ± 20 and 905 ± 115 fs. A non-decaying plateau that extended beyond the pump–probe temporal range was also included to fit the data.

TABLE I. Fit values for cluster dynamics at 15 750 cm^{-1} (635 nm). Time constants and standard deviations obtained from fitting transient dynamics from femtosecond fsTA experiments.

Amplitude	Time constant (fs)
0.003 1[a]	20 ± 5
−0.001 3	120 ± 20
−0.000 17	905 ± 115
−0.000 15	>100 000

[a]A growth component.

Each time constant represents the average decay time of the initially excited carriers; thus, the electronically excited charge carriers thermalize through two different decay channels within the first picosecond following excitation and then continue to relax via a third decay process that persists beyond the experimental window of 150 ps. Fit constants are summarized in Table I. In general, the associated decay processes are consistent with previous ultrafast spectroscopy measurements on quantum-confined gold MPCs. Thus, we attribute the ≈100 and ≈900 fs decays to series of internal conversion steps, which may include a ligand-to-metal core charge transfer process (900 fs).

In addition to time-dependent changes in the transient signal amplitudes, temporal modulations to the GSB detection frequencies were also apparent in Fig. 2(a); the transient spectra were corrected for any pulse chirp. This time-dependent GSB frequency shift is illustrated by Fig. 3, which shows three transient spectra of $Au_{38}(SC_6H_{13})_{24}$ following 15 870 cm^{-1} (630 nm) excitation. At a pump–probe time delay of 100 fs, the excited population is fit by a single Gaussian function at 15 820 cm^{-1} [Fig. 3(a)]. At 250 fs, a lower frequency component (15 625 cm^{-1}) is apparent, requiring two Gaussian functions to fit the spectrum. This low-frequency signal dominates the transient spectra by 1000 fs and persists for the

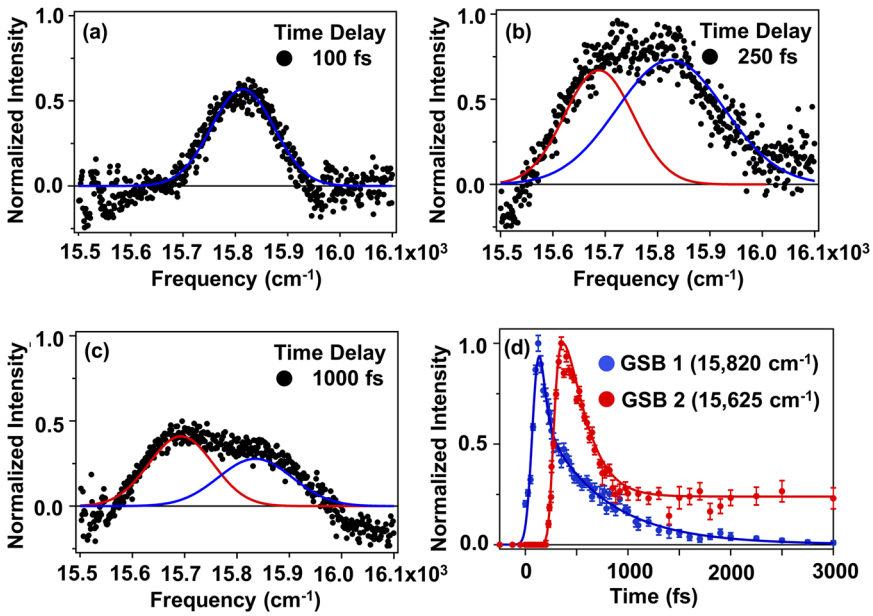

FIG. 3. Transient absorption spectra that show the evolution of the two bleach components across three pump–probe time delays: (a) 100, (b) 250, and (c) 1000 fs. The higher and lower frequency components are shown in blue and red, respectively. Each component was obtained by fitting the transient spectra to a Gaussian function. Transient spectra were normalized to the maximum intensity across the pump–probe time delay series. (d) Overlay of the time-dependent transient bleach amplitudes monitored at 15 820 cm^{-1} (blue) and 15 625 cm^{-1} (red). The overlay demonstrates the delayed onset at buildup of the lower energy bleach signal.

TABLE II. Fit values for the two bleach component amplitudes. Time constants and standard deviations obtained from fitting transient amplitudes from femtosecond fsTA experiments.

Component 1 (15 820 cm^{-1})		Component 2 (15 624 cm^{-1})	
Amplitude	Time constant (fs)	Amplitude	Time constant (fs)
0.0015[a]	30 ± 5	0.0012[a]	80 ± 25
−0.0029	110 ± 45	−0.0014	175 ± 60
−0.0006	720 ± 100	−0.0001	>100 000

[a]A growth component.

remainder of the measurement [Figs. 3(b) and 3(c)]. These results reflect the electronic state-to-state conversion of the excited charge carriers.

To better understand the nature of the state-to-state interconversion process, normalized amplitudes of both peaks were plotted vs the pump–probe time delay in Fig. 3(d); non-normalized amplitudes are plotted in Fig. S3. It was apparent that the 15 625 cm^{-1} bleach component exhibited a significantly delayed (220 fs, with respect to time zero) first-order growth τ_g = 80 ± 25 fs. This delayed buildup of the 15 625 cm^{-1} bleach signal suggests that these states are populated through the decay of the initially excited states at 15 820 cm^{-1}. The high-frequency bleach amplitude (15 820 cm^{-1}) was fit with a consecutive kinetics model that yielded an instantaneous growth and two decay time constants of 110 ± 45 and 720 ± 95 fs. The population transfer from the high- to low-frequency bleach was quantified using a transition-state kinetic model. These data were modeled using a kinetic model adapted from Zewail and Pedersen and are shown in the following equation:

$$M_E(t) = \frac{k_1}{k_1 k_2}[\exp(-k_2 t) - \exp(-k_1 t)], \quad (1)$$

where $M_E(t)$ denotes the molecular response function and a biexponential rise and decay, k_1 and k_2, where the faster one is the growth and the slower one is the decay.[55] Using this model, we determine that the low-frequency bleach (15 625 cm^{-1}) exhibits an 80 ± 25 fs growth, which is within the error of the 110 ± 45 fs decay of the high-frequency component (Table II). The good agreement of these two time constants is consistent with our interpretation that population transfer occurs between the two states represented by the bleach signals at 15 820 and 15 625 cm^{-1}. The 15 820 cm^{-1} signal decays to form the one detected at 15 625 cm^{-1}. We note that the apparent transition state that mediates conversion from 15 820 to 15 625 cm^{-1} detection does not result in complete conversion. The low-amplitude 720 ± 100 fs decay observed for the 15 820 cm^{-1} signal suggests a bifurcation of the transition state that mediates multiple relaxation channels.

Next, the use of 2DES to identify excited states involved in the state-to-state internal conversion process is described. 2DES is better suited to disentangle state-to-state dynamics among the electronic manifold than fsTA because of the inherent excitation-detection correlation of the multi-dimensional method. Because 2DES combines ultrafast temporal resolution with spectral correlations, it can also be used to resolve dynamic peak shape evolution.[56] The state specificity afforded by transient 2DES is shown in Fig. 4, where maps obtained for several pump–probe waiting times spanning the range from

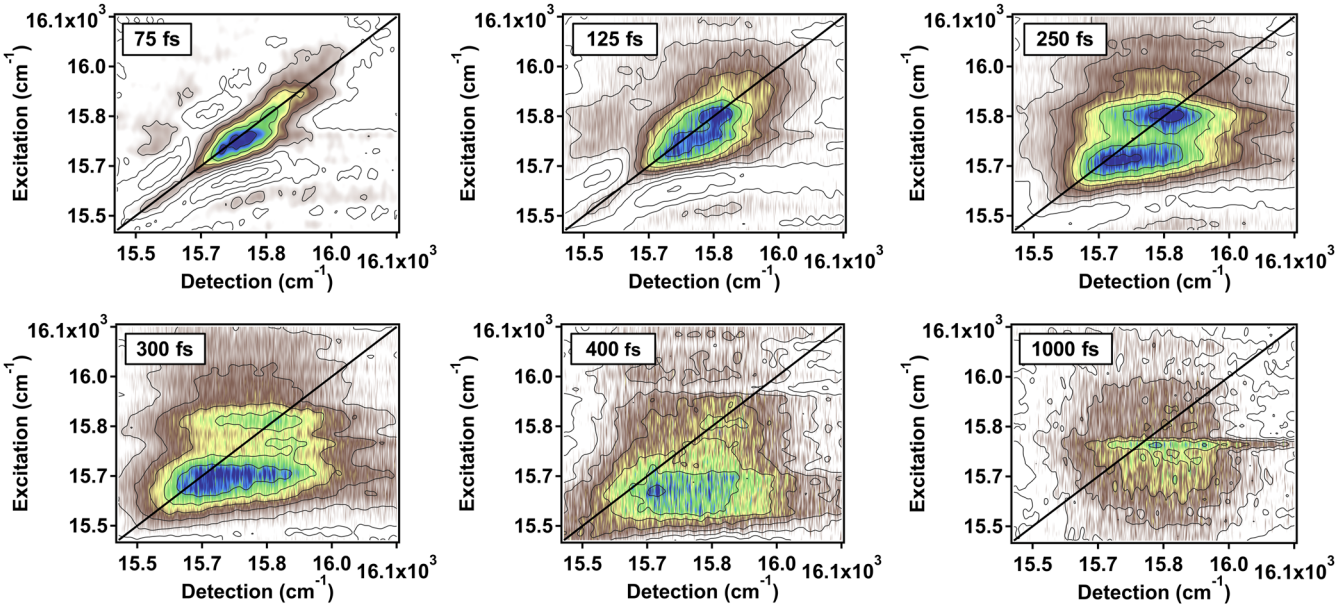

FIG. 4. Ultrafast transient 2DES maps that illustrate dynamic peak evolution recorded at different pump–probe waiting times (T_w) from 75 to 1000 fs. The false color images were used for the maps with blue corresponding to ground state bleaching and were normalized to the maximum signal across the entire time series. At early times (75–125 fs), transient signals are mainly distributed along the 2DES diagonal. By T_w = 250 fs, off-diagonal signals emerge, reflecting state-to-state carrier transfer. Thermalization is observed by 1000 fs, as shown by the circular 2DES peak shape.

75 to 1000 fs are presented. Figure 4 shows the evolution of an initially strongly correlated GSB signal distributed along the diagonal to a circular peak shape at a central excitation-detection frequency of ≈15 800 cm^{-1}. This time-dependent evolution from structured to circular peak shapes represents spectral diffusion.[57] This spectral diffusion is illustrated in Fig. S4, which shows the centerline-slope analysis of the 2DES data plots acquired at specific pump–probe waiting times spanning hundreds of femtoseconds to picoseconds. Insight into state-specific dynamics can be gained by analyzing the 2DES maps at times intermediate to the strongly correlated and thermally randomized regimes. For example, at a pump–probe waiting time of 250 fs, the GSB is shifted off-diagonal, and multiple transient fine-structure states are detected, distributed along the excitation axis spanning a frequency range of ≈600 cm^{-1}. Figure S5 shows a single 2DES map at T_w = 200 fs and its corresponding excitation spectrum plotted from 15 600 to 16 100 cm^{-1}. The solid black line in Fig. S5 denotes the vertical slice taken from the transient 2DES map to plot the fine-structure spectrum. The excitation spectrum includes four peaks that were each fit to a single Gaussian function to determine their frequency position and amplitude. The data in Fig. 4 convey the dynamic evolution of the MPC transient spectra, progressing from an elongated diagonal to off-diagonal fine-structure transitions and finally to a circular shape. This progression qualitatively depicts the evolution from highly correlated fine-structure excitations within the electronic manifold, the internal state-to-state conversion, and finally thermalization of the manifold through electron-vibrational coupling. The timescale for the transformation from a diagonal to circular peak shape was complementary to the sub-picosecond relaxation rates measured from femtosecond TA.

To further analyze the fine-structure peaks shown in Fig. 4 and obtain ultrafast relaxation dynamics in metal clusters, excitation-detection line spectra from several pump–probe waiting times are plotted in Fig. 5. At early time delays (T_w = 75 fs), the excitation-detection spectra are dominated by higher frequency transitions [Fig. 5(a)]. However, the line spectra in Figs. 5(b) and 5(c) show that the relative amplitudes of the fine-structure peaks change as pump–probe waiting times increase to 300 fs. The line spectra in Fig. 5 show an instantaneous non-zero amplitude for all fine-structure peaks at the shortest pump–probe delay times. However, the low-energy peak builds up within a few hundred femtoseconds. It is important to note that all of the transitions are initially populated upon femtosecond excitation; the time dependence of the excitation line spectra reflects the dominant oscillator strength of the high-energy excitation. This effect is most clearly seen by analyzing the time dependences of the 2DES amplitudes at multiple excitation/detection correlation frequencies, which were isolated at

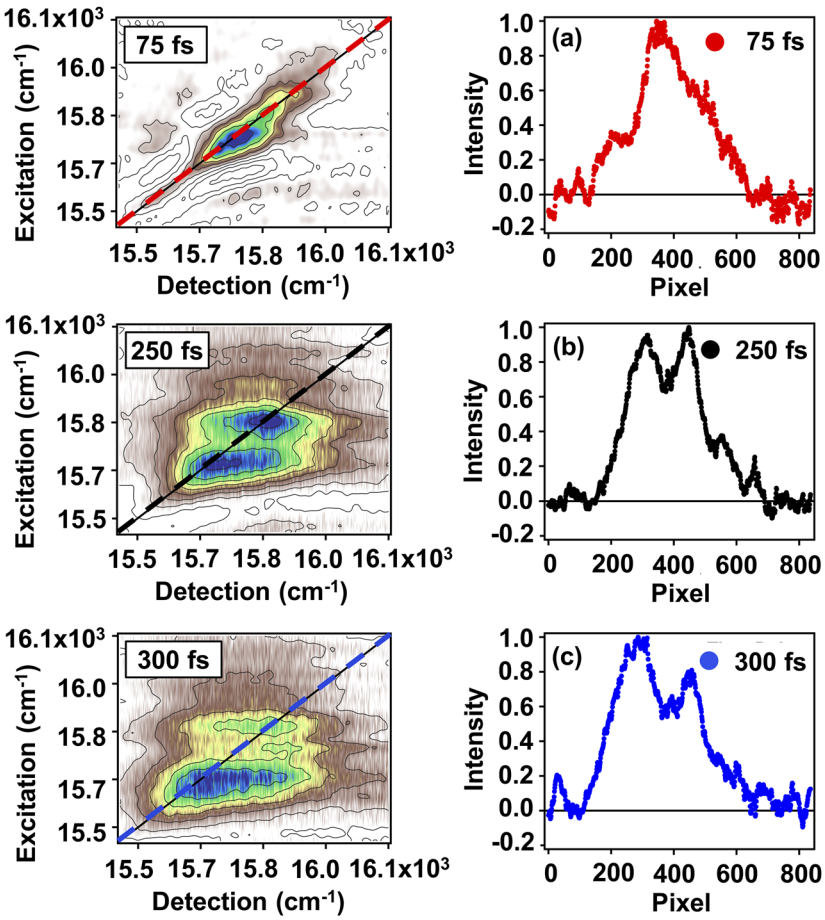

FIG. 5. Transient 2DES maps (left) and excitation-detection line spectra (right) at pump–probe waiting times of (a) 75, (b) 250, and (c) 300 fs. The dashed lines represent the slice of the 2DES maps used to plot the line spectra.

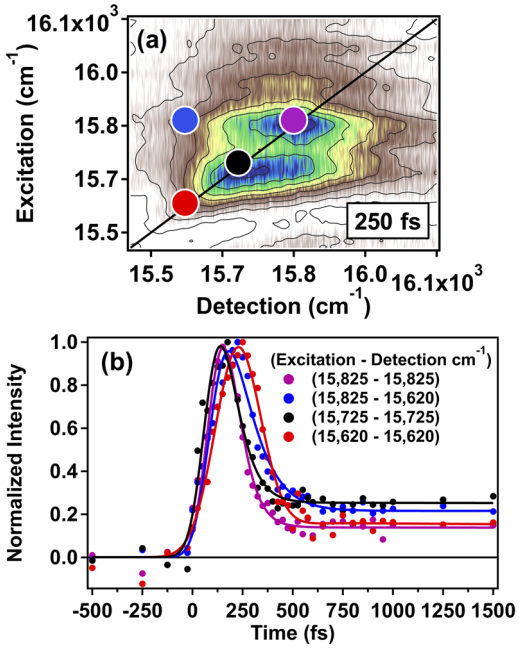

FIG. 6. (a) Transient 2DES map at waiting time T_w = 250 fs and (b) corresponding time-dependent signal amplitudes monitored at different excitation-detection frequencies that span the range of the fine-structure states. Time-dependent transient signal amplitudes (circles) plotted normalized to the maximum amplitude of the time series. The solid lines represent fits to a series of exponentials convoluted with the Gaussian instrument response.

three different excitation-detection frequencies along the diagonal (15 620, 15 725, and 15 825 cm^{-1}), and an off-diagonal excitation/detection frequency (15 825/15 620 cm^{-1}), denoted by filled circles in Fig. 6(a). Each trace was fit to a series of exponentials convoluted with the Gaussian instrument response. Fit values are listed in Table III. Along the diagonal, the two higher excitation frequencies have nearly identical dynamics with an instantaneous growth (≈10 fs), rapid ≈100 fs decay, and a long-lived decay that exceeds the 2DES temporal range (>15 000 fs). However, the dynamics at 15 620 cm^{-1} exhibited a slower growth time constant (75 ± 10 fs) and a slightly slower decay (150 ± 20 fs) than the 15 725 and 15 825 cm^{-1} diagonal frequencies. The significance of this observation is twofold: (1) it illustrates the internal conversion from the higher energy excitation to the lower energy resonance and (2) it reflects the larger oscillator strength for the two transitions at higher energy; all three transitions are resonant within the laser bandwidth.

The time dependence of the signals measured off-diagonal (15 825/15 620 cm^{-1} cross peak) is of particular interest because they uniquely resolve state-to-state relaxation processes. The off-diagonal trace yielded a growth (65 ± 15 fs) and decay (160 ± 35 fs). The excitation-detection correlation afforded by the 2DES method allows for the quantification of state-to-state relaxation dynamics, which cannot directly be obtained from femtosecond TA experiments. As such, the amplitude dynamics at 15 825 and 15 620 cm^{-1} measured by 2DES provided quantitative evidence of femtosecond population transfer from the higher-to-lower-energy fine-structure states in $Au_{38}(SC_6H_{13})_{24}$ MPCs.

These results demonstrate the ability of 2DES to map energy flow through near-degenerate fine-structure states and to quantify rapid internal conversion of electronic charge carriers on the sub-100 fs timescale. Thus, 2DES readily provides state-specific information regarding ultrafast relaxation dynamics in structurally precise metal nanoclusters that cannot be obtained from traditional transient absorption experiments, which are limited by spectrally congested spectra. Thus, careful consideration of each transition is needed to fully describe structure-dependent relaxation dynamics in $Au_{38}(SC_6H_{13})_{24}$ MPCs.

The state-to-state relaxation mechanism of $Au_{38}(SC_6H_{13})_{24}$ can be understood by comparing the 2DES data to previously reported density functional theory (DFT) and Kohn–Sham electronic state descriptions.[34,54,58] As stated previously in this section, the charge transfer resonance probed in this experiment consists of several mixed core and semiring transitions. The highest oscillator strength transition is $HOMO_{-12/-13} \rightarrow LUMO$, which has significant Au–S ligand band character. The lower-lying $HOMO_{-4/-6} \rightarrow LUMO$ transitions are localized throughout the metal core and ligand band. Thus, our data suggest that absorption occurs through excitation of the higher-lying ligand band states ($HOMO_{-12/-13} \rightarrow LUMO$) at 15 825–15 725 cm^{-1}, and the excited hole carriers internally convert into the lower-lying $HOMO_{-4/-6} \rightarrow LUMO$ states (15 625 cm^{-1}) that have mixed semiring and core orbital contributions. This relaxation mechanism is depicted in Fig. 7. First, absorption occurs predominately in the ligand band ($HOMO_{-12/-13} \rightarrow LUMO$). Second, excited hole carriers internally relax into the mixed $HOMO_{-4/-6}$ states by internal conversion, which is evidenced by the 2DES-detected electronic fine-structure states. The 225 cm^{-1} energy difference between excitation-detection frequencies is in good agreement with theoretical predictions of the energy gap separating the $HOMO_{-12/-13}$ and $HOMO_{-4/-6}$ manifold. Next, the carriers relax by $HOMO_{-4/-6}$ to HOMO hole transfer over the next several hundred

TABLE III. Fit values for cluster dynamics from 2DES experiments. Time constants and standard deviations obtained from fitting transient dynamics from femtosecond 2DES experiments.

Frequency (cm^{-1})	A_1	T_1 (fs)	A_2	T_2 (fs)	A_{inf}	T_3 (fs)
(15 620, 15 620)	−5.8[a]	75 ± 10	14.9	150 ± 20	0.16	>15 000
(15 725, 15 725)	−8.2[a]	12 ± 5	9.4	90 ± 15	0.25	>15 000
(15 825, 15 825)	−9.6[a]	15 ± 5	8.5	80 ± 10	0.14	>15 000
(15 825, 15 620)	−6.6[a]	65 ± 15	7.8	160 ± 35	0.21	>15 000

[a]A growth component.

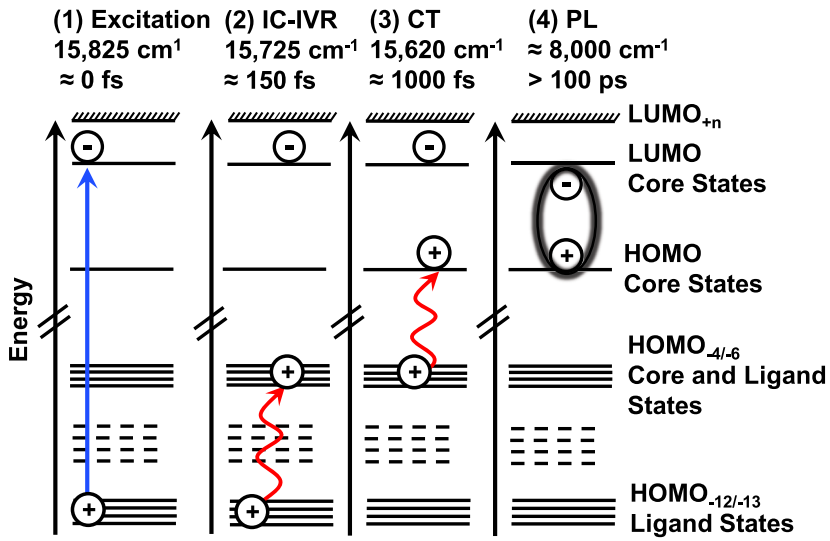

FIG. 7. Electronic charge carrier relaxation model resulting from 630-nm excitation of the charge transfer transition in $Au_{38}(SC_6H_{13})_{24}$. Photo-generated holes undergo a series of state-to-state relaxation steps: (1) absorption occurs predominately within the ligand band; (2) excited holes internally relax through a manifold of heavily mixed ligand-core states, including $HOMO_{-12/-13}$ to $HOMO_{-4/-6}$; (3) carriers then undergo CT from mixed $HOMO_{-4/-6}$ to metal core-based HOMO states over the next 1000 fs; and (4) electron–hole recombination through radiative decay occurs over timescales exceeding the >150 ps range of the measurements.

femtoseconds. Finally, the excited charge carriers undergo radiative recombination through the core-localized states over several hundred picoseconds, persisting beyond our measurement range. An alternative explanation for the observed transient diagonal and cross peaks invokes vibronic transitions. The 2DES features are attributed to distinct electronic excitations based on the excellent agreement between experimental spectra and calculated electronic excitation energies.[34,54,58] In future research, comparisons between cross and co-polarized pump and probe beams may provide a more definitive measurement-based determination.[59]

We note that previous TA experiments by Zhou *et al.* suggest that the picosecond decay corresponds to metal-to-ligand charge transfer.[20] However, our experiments selectively pump and probe the heavily mixed transition at 630 nm, where the largest oscillator strength transition has significant semiring (i.e., ligand band) character. Thus, it is likely that ligand-based states contribute rather significantly to the initial excitation and govern relaxation. This is consistent with TDPL measurements, where both Au–Au core and Au–S semiring vibrational modes mediate nonradiative relaxation in $Au_{38}(SC_{12}H_{25})_{24}$. Furthermore, the long-lived transient signal from our fsTA measurements likely corresponds to radiative carrier recombination on longer timescales. Time-dependent DFT calculations by Dimuthu *et al.* suggest that photoluminescence predominately occurs through a HOMO–LUMO transition comprised of core-localized orbitals.[60] However, both the inorganic Au–S semiring and metal core play integral roles in governing nonradiative relaxation dynamics in $Au_{38}(SR)_{24}$ MPCs.[61] Taken together, these results suggest that the complex interplay between the inorganic semiring and core structures, along with the initial excitation conditions, plays an integral role in governing electronic charge relaxation in structurally precise $Au_{38}(SC_6H_{13})_{24}$ MPCs.

IV. CONCLUSIONS

Here, femtosecond transient absorption and two-dimensional electronic spectroscopy measurements were employed to investigate electronic charge carrier relaxation dynamics in quantum-confined $Au_{38}(SC_6H_{13})_{24}$ MPCs. Identification of rapid internal conversion and hole transfer dynamics were resolved through time-dependent amplitudes of fsTA differential spectra and 2DES-detected evolution of electronic fine-structure states. From fsTA, single-wavelength dynamics yielded rapid 120 ± 20 fs and slower 905 ± 115 fs decay time constants, which are consistent with previous fsTA experiments on gold MPCs. The time-dependent amplitudes of two Gaussian components fit to the differential fsTA spectra indicated rapid peak interconversion between the two components, which suggests that photoexcited charge carriers rapidly transfer between different states within 100 fs. The excitation-detection spectra and transient dynamics from 2DES diagonal and off-diagonal cross peaks indicated that the state-to-state dynamics could be identified and resolved on the sub-100 fs timescale. 2DES data agreed well with previously published DFT calculations, suggesting a stepwise $HOMO_{-12/-13}$ to $HOMO_{-4/-6}$ to HOMO charge carrier relaxation model in $Au_{38}(SC_6H_{13})_{24}$ MPCs. The relaxation mechanism is described by four sequential steps: (1) absorption within the ligand charge transfer band, (2) internal conversion of hole carriers within 100 fs from $HOMO_{-12/-13}$ to $HOMO_{-4/-6}$, (3) hole relaxation from $HOMO_{-4/-6}$ to HOMO within 1000 fs, and (4) electron–hole recombination persisting over longer timescales. These results demonstrate the ability of 2DES to provide ultrafast transient excitation-detection correlations that can be used to resolve state-to-state energy relaxation in structurally precise nanoclusters. Future studies combining femtosecond 2DES and controlled structural modifications to specific nanocluster domains show great potential for understanding structure-dependent electronic relaxation dynamics.

SUPPLEMENTARY MATERIAL

See the supplementary material for Figs. S1–S5, which include additional transient spectra.

ACKNOWLEDGMENTS

This work was supported by an award from the National Science Foundation (Grant No. CHE-1904876). The authors thank Dr. Stefan Knoppe for providing the MPC samples used in this study.

DATA AVAILABILITY

The data that support the findings of this study are available from the corresponding author upon reasonable request.

REFERENCES

[1]T. D. Green, P. J. Herbert, C. Yi, C. Zeng, S. McGill, R. Jin, and K. L. Knappenberger, Jr., J. Phys. Chem. C **120**, 17784–17790 (2016).
[2]L. J. Williams, P. J. Herbert, M. A. Tofanelli, C. J. Ackerson, and K. L. Knappenberger, Jr., J. Chem. Phys. **150**, 101102 (2019).
[3]P. J. Herbert and K. L. Knappenberger, Jr., Small **17**, 2004431 (2021).
[4]P. J. Herbert, M. A. Tofanelli, C. J. Ackerson, and K. L. Knappenberger, Jr., J. Phys. Chem. C **125**, 7267–7275 (2021).
[5]M. Valden, X. Lai, and D. W. Goodman, Science **281**, 1647–1650 (1998).
[6]G. Li and R. Jin, Acc. Chem. Res. **46**, 1749–1758 (2013).
[7]O. Lopez-Acevedo, K. A. Kacprzak, J. Akola, and H. Häkkinen, Nat. Chem. **2**, 329–334 (2010).
[8]J. F. Hainfeld, Science **236**, 450–453 (1987).
[9]S. Knoppe, M. Vanbel, S. van Cleuvenbergen, L. Vanpraet, T. Bürgi, and T. Verbiest, J. Phys. Chem. C **119**, 6221–6226 (2015).
[10]N. Van Steerteghem, S. Van Cleuvenbergen, S. Deckers, C. Kumara, A. Dass, H. Häkkinen, K. Clays, T. Verbiest, and S. Knoppe, Nanoscale **8**, 12123–12127 (2016).
[11]Y. Liu, H. Tsunoyama, T. Akita, and T. Tsukuda, Chem. Commun. **46**, 550–552 (2010).
[12]Y. Liu, H. Tsunoyama, T. Akita, S. Xie, and T. Tsukuda, ACS Catal. **1**, 2–6 (2011).
[13]P. D. Jadzinsky, G. Calero, C. J. Ackerson, D. A. Bushnell, and R. D. Kornberg, Science **318**, 430–433 (2007).
[14]M. W. Heaven, A. Dass, P. S. White, K. M. Holt, and R. W. Murray, J. Am. Chem. Soc. **130**, 3754–3755 (2008).
[15]R. Jin, Nanoscale **2**, 343–362 (2010).
[16]Y. Niihori, S. Hashimoto, Y. Koyama, S. Hossain, W. Kurashige, and Y. Negishi, J. Phys. Chem. C **123**, 13324–13329 (2019).
[17]C. Liu, T. Li, G. Li, K. Nobusada, C. Zeng, G. Pang, N. L. Rosi, and R. Jin, Angew. Chem., Int. Ed. **54**, 9826–9829 (2015).
[18]S. Tian, Y.-Z. Li, M.-B. Li, J. Yuan, J. Yang, Z. Wu, and R. Jin, Nat. Commun. **6**, 8667–8672 (2015).
[19]H. Qian, W. T. Eckenhoff, Y. Zhu, T. Pintauer, and R. Jin, J. Am. Chem. Soc. **132**(24), 8280–8281 (2010).
[20]M. Zhou, S. Tian, C. Zeng, M. Y. Sfeir, and R. Jin, J. Phys. Chem. C **121**, 10686–10693 (2017).
[21]M. Zhou, T. Higaki, G. Hu, M. Y. Sfeir, Y. Chen, D. Jiang, and R. Jin, Science **364**, 279–282 (2019).
[22]T. D. Green, C. Yi, C. Zeng, R. Jin, S. McGill, and K. L. Knappenberger, Jr., J. Phys. Chem. **118**, 10611–10621 (2014).
[23]S. A. Miller, J. M. Womick, J. F. Parker, R. W. Murray, and A. M. Moran, J. Phys. Chem. C **113**, 9440–9444 (2009).
[24]H. Qian, M. Y. Sfeir, and R. Jin, J. Phys. Chem. C **114**, 19935–19940 (2010).
[25]M. S. Devadas, J. Kim, E. Sinn, D. Lee, T. Goodson III, and G. Ramakrishna, J. Phys. Chem. C **114**, 22417–22423 (2010).
[26]T. D. Green and K. L. Knappenberger, Jr., Nanoscale **4**, 4111–4118 (2012).
[27]C. Yi, M. A. Tofanelli, C. J. Ackerson, and K. L. Knappenberger, Jr., J. Am. Chem. Soc. **135**, 18222–18228 (2013).
[28]S. Mustalahti, P. Myllyperkiö, T. Lahtinen, K. Salorinne, S. Malola, J. Koivisto, H. Häkkinen, and M. Pettersson, J. Phys. Chem. C **118**, 18233–18239 (2014).
[29]S. Mustalahti, P. Myllyperkiö, S. Malola, T. Lahtinen, K. Salorinne, J. Koivisto, H. Häkkinen, and M. Pettersson, ACS Nano **9**, 2328–2335 (2015).
[30]B. Varnholt, R. Letrun, J. J. Bergkamp, Y. Fu, O. Yushchenko, S. Decurtins, E. Vauthey, S.-X. Liu, and T. Bürgi, Phys. Chem. Chem. Phys. **17**, 14788–14795 (2015).
[31]C. Yi, H. Zheng, L. M. Tvedte, C. J. Ackerson, and K. L. Knappenberger, Jr., J. Phys. Chem. C **119**, 6307–6313 (2015).
[32]C. Yi, H. Zheng, P. J. Herbert, Y. Chen, R. Jin, and K. L. Knappenberger, Jr., J. Phys. Chem. C **121**, 24894–24902 (2017).
[33]P. J. Herbert, C. Yi, W. S. Compel, C. J. Ackerson, and K. L. Knappenberger, Jr., J. Phys. Chem. C **122**, 19251–19258 (2018).
[34]O. Lopez-Acevedo, H. Tsunoyama, T. Tsukuda, H. Häkkinen, and C. M. Aikens, J. Am. Chem. Soc. **132**, 8210–8218 (2010).
[35]J. D. Hybl, A. W. Albrecht, S. M. Gallagher Faeder, and D. M. Jonas, Chem. Phys. Lett. **297**, 307–313 (1998).
[36]J. D. Hybl, A. Albrecht Ferro, and D. M. Jonas, J. Chem. Phys. **115**, 6606 (2001).
[37]T. Brixner, T. Mančal, I. V. Stiopkin, and G. R. Fleming, J. Chem. Phys. **121**, 4221 (2004).
[38]T. Brixner, J. Stenger, H. M. Vaswani, M. Cho, R. E. Blankenship, and G. R. Fleming, Nature **434**, 625–628 (2005).
[39]J. A. Myers, K. L. M. Lewis, F. D. Fuller, P. F. Tekavec, C. F. Yocum, and J. P. Ogilvie, J. Phys. Chem. Lett. **1**, 2774–2780 (2010).
[40]M. Maiuri, J. Réhault, A.-M. Carey, K. Hacking, M. Garavelli, L. Lüer, D. Polli, R. J. Cogdell, and G. Cerullo, J. Chem. Phys. **142**, 212433 (2015).
[41]F. Milota, J. Sperling, A. Nemeth, T. Mančal, and H. F. Kauffmann, Acc. Chem. Res. **42**, 1364–1374 (2009).
[42]Y. Lee, S. Das, R. M. Malamakal, S. Meloni, D. M. Chenoweth, and J. M. Anna, J. Am. Chem. Soc. **139**, 14733–14742 (2017).
[43]S. Rafiq, M. J. Bezdek, M. Koch, P. J. Chirik, and G. D. Scholes, J. Am. Chem. Soc. **140**, 6298–6307 (2018).
[44]D. B. Turner, Y. Hassan, and G. D. Scholes, Nano Lett. **12**, 880–886 (2012).
[45]R. D. Mehlenbacher, T. J. McDonough, M. Grechko, M.-Y. Wu, M. S. Arnold, and M. T. Zanni, Nat. Commun. **6**, 6732 (2015).
[46]J. W. Jarrett, C. Yi, T. Stoll, J. Réhault, A. Oriana, F. Branchi, G. Cerullo, and K. L. Knappenberger, Jr., Nanoscale **9**, 4572–4577 (2017).
[47]L. Wang, N. E. Williams, E. W. Malachosky, J. P. Otto, D. Hayes, R. E. Wood, P. Guyot-Sionnest, and G. S. Engel, ACS Nano **11**, 2689–2696 (2017).
[48]L. Guo, M. Wu, T. Cao, D. M. Monahan, Y.-H. Lee, S. G. Louie, and G. R. Fleming, Nat. Phys. **15**, 228–232 (2019).
[49]T. Stoll, E. Sgrò, J. W. Jarrett, J. Réhault, A. Oriana, L. Sala, F. Branchi, G. Cerullo, and K. L. Knappenberger, Jr., J. Am. Chem. Soc. **138**, 1788–1791 (2016).
[50]S. Knoppe, J. Boudon, I. Dolamic, A. Dass, and T. Bürgi, Anal. Chem. **83**, 5056–5061 (2011).
[51]M. A. Steves, H. Zheng, and K. L. Knappenberger, Jr., Opt. Lett. **44**, 2117–2120 (2019).
[52]E. M. Grumstrup, S.-H. Shim, M. A. Montgomery, N. H. Damrauer, and M. T. Zanni, Opt. Express **15**, 16681–16689 (2007).
[53]F. D. Fuller and J. P. Ogilvie, Annu. Rev. Phys. Chem. **66**, 667–690 (2015).
[54]R. D. Senanayake, E. B. Guidez, A. J. Neukirch, O. V. Prezhdo, and C. M. Aikens, J. Phys. Chem. C **122**, 16380–16388 (2018).
[55]S. Pedersen and A. H. Zewail, Mol. Phys. **89**, 1455–1502 (1996).
[56]A. Tokmakoff, J. Phys. Chem. A **104**, 4247–4255 (2000).
[57]S. T. Roberts, J. J. Loparo, and A. Tokmakoff, J. Chem. Phys. **125**, 084502 (2006).
[58]Y. Pei, Y. Gao, and X. C. Zeng, J. Am. Chem. Soc. **130**, 7830–7832 (2008).
[59]Y. Song, A. Schubert, E. Maret, R. K. Burdick, B. D. Dunietz, E. Geva, and J. P. Ogilvie, Chem. Sci. **10**, 8143–8153 (2019).
[60]K. L. Dimuthu, M. Weerawardene, E. B. Guidez, and C. Aikens, J. Phys. Chem. C **121**, 15416–15423 (2017).
[61]P. J. Herbert, C. J. Ackerson, and K. L. Knappenberger, Jr., J. Phys. Chem. Lett. **12**, 7531–7536 (2021).